PAPER

Mechanism of coupled phase/morphology transformation of 2D manganese oxides through Fe galvanic exchange reaction†

Raquel Aymerich-Armengol, [ID] *[a] Paolo Cignoni, [ID] [b] Petra Ebbinghaus,[a] Julia Linnemann, [ID] [b] Martin Rabe, [ID] [a] Kristina Tschulik, [ID] [b] Christina Scheu [ID] *[a] and Joohyun Lim [ID] *[c]

Nanostructured manganese oxides have a rich variety of morphologies and crystal phases which can undergo transformations during synthesis and application. Although these structural features are crucial for their performance, the mechanisms behind such transitions are not well understood. Herein, we describe the mechanism of transformation from layered 2D δ-MnO_2 nanosheets to the scarcely reported γ-MnO_2 nanocone morphology. Despite the common purpose of introducing Fe dopants to enhance the conductivity of layered manganese oxides, the Fe galvanic exchange reaction was found responsible for such coupled phase/morphology transition. Electrochemical characterization confirmed a distinct electrochemical behaviour of the nanocones, emphasizing the need to unravel the mechanism of 2D MnO_2 transformation. Such mechanistic insights were gained by systematic and rigorous electron microscopy studies. The effect of the local chemical composition was determined by energy dispersive X-ray spectroscopy while electron energy loss spectroscopy unravelled the key influence of the oxidation state of Mn ions within nanosheets and nanocones. We propose and demonstrate a Mn^{2+}-mediated oxidative mechanism of coupled morphology/phase transformation subjected to the equilibrium of Fe and Mn ions during galvanic exchange reaction. These findings contribute to the understanding of the growth and morphology/phase transformations of manganese oxide nanostructures, providing insights for the rational design of nanomaterials.

Introduction

Nanostructured manganese oxides (MnO_2) are promising candidates for energy storage (*e.g.* batteries and super-capacitors),[1] environmental (*e.g.* pollutant removal),[2] and catalysis applications (*e.g.* oxygen evolution reaction).[3] Their properties are strongly dependent on the structure, which shows high complexity due to the variety of nanomorphologies, crystal structures (distinguishing between tunnel- and layer-like structure types), chemical compositions and stoichiometries.[3–5]

The introduction of dopants is conducted to further improve the properties of MnO_2.[5,6] First described by Oh *et al.*,[7] the galvanic exchange reaction can be performed to introduce Fe dopant in nanostructured oxides, including 2D MnO_2 nanosheets.[8] The presence of Fe enhances the electric conductivity of the MnO_2 material, which is a requirement for electrochemical applications. According to previous reports, dopant percentages of Fe up to 5 at% optimized the specific capacitance of MnO_2.[9–11]

Morphology and/or phase transitions can occur not only during synthesis, but also during post-synthesis procedures such as dopant modification and application of the nanostructures.[12,13] It has been reported that the presence of certain cations can stabilize specific crystal structures, thus causing phase transformations that are often coupled with structural changes. This is the case for the layer-to-tunnel polymorphic transitions of MnO_2, which benefit from the presence of cations of similar size occupying the tunnel void.[14–16] Specific examples of layer-to-tunnel transformations are those triggered by the sorption of Mn^{2+}. Two mechanisms were hypothesized to explain them: on the one hand, auto-catalytic oxidation of the adsorbed Mn^{2+} on the MnO_2 surface would account for transition to Mn^{3+} enriched oxides.[17] On the other hand, comproportionation between Mn^{2+} ions and Mn^{4+} of MnO_2 would also explain Mn^{3+} presence.[18,19]

Although understanding these transformations is of upmost importance for the design of high-performing materials, the

[a]Max-Planck-Institut für Eisenforschung GmbH, Max-Planck-Straße 1, 40237, Düsseldorf, Germany. E-mail: r.aymerich@mpie.de; c.scheu@mpie.de

[b]Faculty of Chemistry and Biochemistry, Chair of Analytical Chemistry II, Ruhr University Bochum, 44780 Bochum, Germany

[c]Department of Chemistry, Institute for Molecular Science and Fusion Technology, Kangwon National University, Chuncheon, Gangwon, 24341, Republic of Korea. E-mail: jlim@kangwon.ac.kr

mechanisms behind them are not yet completely unravelled.[20] For instance, Tu *et al.* observed a coupled phase/morphology transition upon Mn^{2+} addition from layered birnessite to several different MnO_2 structures.[17] However, their synthesis methodology required several days and the exact mechanism behind the layer-to-tunnel transformation could not be proven due to lack of local structural analyses. Among the nanostructures yielding from the layer-to-tunnel transformation, MnO_2 nanocones were obtained. The nanocones consist of a hexagonal pyramid morphology with faceted faces and a ramsdellite γ-MnO_2[21] or the closely related ε-MnO_2[22] crystal structure. This nanostructure has since rarely been reported either arising from self-assembly of α-MnOOH nanorods[21,23] or other direct wet chemical synthesis.[22] Furthermore, no electrochemical structure–property relationship study was pursued for the nanocone structure.

In this work, we achieve rapid phase transformation of layered MnO_2 to γ-MnO_2 nanocones by *in situ* generation of Mn defects and Mn^{2+} ions within 2D manganese oxide nanosheets using Fe galvanic exchange reaction. To investigate the phase transformation mechanism, extensive local structural and chemical characterization of the nanostructures was conducted by electron microscopies (scanning electron microscopy (SEM), (scanning) transmission electron microscopy ((S)TEM) and spectroscopic techniques (energy dispersive X-ray (EDS), electron energy loss spectroscopy (EELS) and Raman spectroscopy). The results allowed us to describe a Mn^{2+}-mediated oxidative mechanism for the nanosheet to nanocone morphology *via* galvanic exchange reaction. Our findings shed light into the mechanism behind coupled phase/morphology transitions of MnO_2, which is crucial for building structure–property relationships of functional nanomaterials.

Experimental section

Materials

The materials used during synthesis were tetramethylammonium hydroxide (TMAOH, 25 wt% in water, Sigma-Aldrich), hydrogen peroxide (H_2O_2, 30 wt%, Merck), manganese chloride ($MnCl_2 \cdot 4H_2O$, >98%, Sigma-Aldrich), hydrochloric acid (HCl, 37 wt%, VWR), iron sulphate ($FeSO_4 \cdot 7H_2O$, >98%, Sigma-Aldrich), tetramethylammonium chloride (TMACl, >98%, Sigma-Aldrich) and ethanol (EtOH, >99.8%, Carl Roth).

To prepare the working electrodes 1-methyl-2-pyrrolidone (NMP, >99%, Alfa Aesar) and Nafion® 117 solution ($\approx$5% in mixture of lower aliphatic alcohols, Sigma-Aldrich) were used. The electrolyte for the electrochemical measurements was prepared from potassium sulphate (K_2SO_4, AnalaR NORMA-PUR, VWR).

Synthesis

MnO_2 nanosheets synthesis.[8,24] To prepare $\sim$60 ml of product, a mixture of 43 ml of a solution of 0.6 M TMAOH and 3 wt% H_2O_2 was added slowly to 16 ml of a 0.3 M $MnCl_2 \cdot 4H_2O$ solution. The dark brown mixture was let to stir from 15 h (HMO, 1M-HMO) to 24 h (2M-HMO, 3M-HMO) and was

centrifuged for 8 min at 3800 rpm either immediately (1M-HMO, 2M-HMO) or after 24 h (FMO, 3M-HMO). The supernatant suspension was aggregated with HCl 36 wt% (*ca.* 0.8 ml). This solution was centrifugated for 4 min at 5000 rpm and the aggregates were redispersed in deionized water and in EtOH. Finally, the aggregates in the solution were dried for 6.5 h in an oven preheated at 110 °C and the powder was grinded in an agate mortar.

Fe galvanic exchange.[8] Typically, 0.5 ml of a $FeSO_4 \cdot 7H_2O$ precursor solution of concentration in the range of 2–25 mg ml^{-1} were injected to 5 ml of MnO_2 nanosheets suspension (1 mg ml^{-1}). To test the effect of pH and cations, 1.7×10^{-5} mol of either TMAOH (6 μL) or TMACl (1.8 mg) were added to the MnO_2 solution prior to Fe addition. In all cases, immediately after Fe addition the solution was heated to 90 °C (heating rate 3°C min^{-1}) while stirring for 2 h.

Aging of the materials. After Fe galvanic exchange reaction, the suspension was let to age for 24 h. The materials were subsequently purified with centrifugation and redispersion cycles in deionized water and EtOH.

Electrochemical characterization

Cyclic voltammograms (CVs) were recorded with a three electrodes setup connected to a BioLogic VSP-300 potentiostat. A homemade Ag/AgCl, 3 M KCl electrode ($E = 0.210$ V *vs.* SHE) equipped with 0.5 M K_2SO_4 double junction was used as a reference electrode and a graphite rod ($d = 8$ mm) was used as a counter electrode. The CVs were acquired using an analog scan rate of 25 mV s^{-1} between 0.0 – 0.8 V *vs.* Ag/AgCl, 3 M KCl with a 0.5 M K_2SO_4 solution as an electrolyte. The working electrodes were prepared on a glass slide substrate (0.2 mm thickness, 18 mm diameter) coated with a 200 nm layer of gold and with an 8 nm Ti adhesion layer. 10 μL of a dispersion of 10 mg ml^{-1} of the active material and a 1 mg ml^{-1} of Nafion® in NMP were drop cast in the middle of the electrode slide in four 1.5 μL and two 2.0 μL steps. The functionalized electrodes were loaded in a custom-made teflon cell leaving exposed to the electrolyte solution the central area of the working electrode ($d = 10$ mm).[25] A schematic of the cell is shown in Fig. S1.† The potentials were converted to the SHE scale for graph preparation.

Structural characterization

Electron microscopy. SEM micrographs were acquired in a ZEISS Gemini with an acceleration voltage of 1.5 kV using an in-lens secondary electron detector. High resolution TEM (HRTEM) and scanning transmission electron microscopy high angle annular dark field (STEM-HAADF) were conducted in two FEI Titan Themis 60–300 with a C_s corrector for the objective and condenser lenses, respectively. EDS was performed with the Bruker Super X-EDX detector of the microscopes while EELS was acquired at the probe corrected STEM with a Gatan Quantum ERS energy filter. To check any possible reduction by the electron beam on the thin nanostructures, experiments were performed on nanosheets and nanocones of various thickness. The results can be found on Fig. S2.† Since no severe reduction was

This journal is © The Royal Society of Chemistry 2022

J. Mater. Chem. A, 2022, **10**, 24190–24198 | **24191**

observed for the thinner areas measured, we believe that the difference in oxidation state among nanostructures is not related to the electron beam. To determine the ratios of intensity $I(L_3)/(L_2)$ a double arc tangent step function was applied to subtract the post-edge background.[26]

Raman spectroscopy. The samples were drop cast on a Au substrate and analysed with a LabRAM confocal Raman microscope (Horiba Jobin Yvon, France) using a HeNe laser with $\lambda = 633$ nm, laser power of 0.6 mW for an exposure time of 40 s per measurement and a 1800 groove/mm grating. Olympus objectives of $50\times$ (N. A. 0.5) were used where appropriate.

Inductively coupled plasma mass-spectroscopy (ICP-MS). The Mn ions in solution after conducting galvanic exchange reaction were quantified by ICP measurements in a NexION 300 PerkinElmer spectrometer. To prepare the solutions for analysis, the suspensions of $Fe_xMn_{1-x}O_2$ nanomaterials were centrifuged several times after galvanic exchange reaction. The clear supernatant was diluted 1 : 1000 and then analyzed with the ICP-MS.

Results and discussion

Transformation of MnO_2 through Fe galvanic exchange reaction

2D MnO_2 nanosheets (HMO) were synthesized through a wet chemical reaction and subsequently assembled with protons by adding HCl, as explained in the Experimental section. The electrostatic interaction of the hydrated protons with the negatively charged nanosheets produces 3D assemblies (Fig. 1a) of individual nanosheets (Fig. 1b). Fe dopant was subsequently introduced to the assembled MnO_2 with Fe^{2+} precursor to HMO ratios of 1 : 5, 3 : 5, 5 : 5 and 12.5 : 5 in weight and let 24 h to age. Electron micrographs of these materials, respectively named
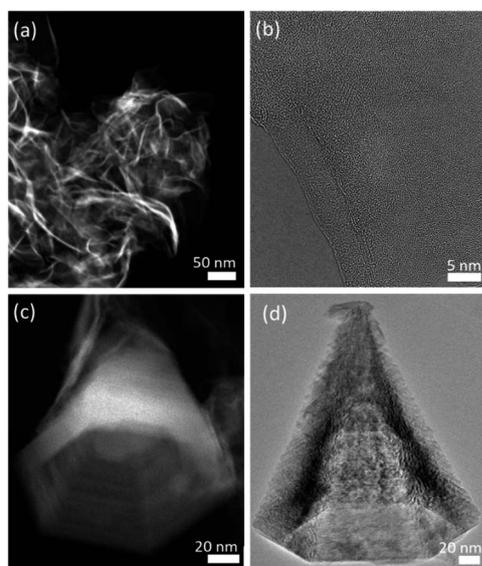

Fig. 1 (a) Scanning transmission electron microscopy high angle annular dark field (STEM-HAADF) micrograph of HMO 3D nanosheets assembly composed by individual nanosheets shown by HRTEM in (b). (c) STEM-HAADF and (d) TEM images of FMO2 hollow nanocones.
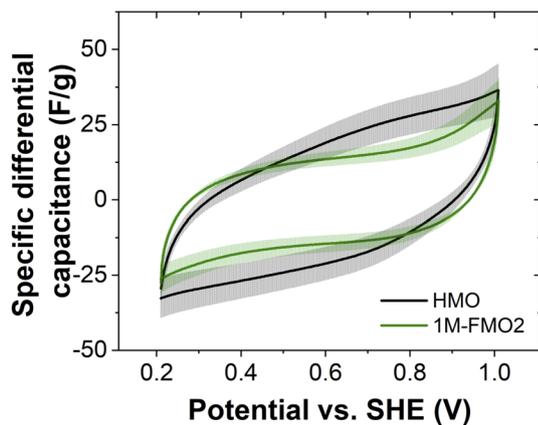
FMO1, FMO2, FMO3 and FMO4, are shown in Fig. S3.† All materials presented similar 3D assemblies of nanosheets.

As demonstrated by Lim et al.,[8] after Fe introduction and reaction at 90 °C the Fe cations are not only present in the interlayer space replacing the hydrated protons but are also partially incorporated to the MnO_2 lattice in Mn substitutional sites by galvanic exchange. For the MnO_2/Mn^{2+} and Fe^{3+}/Fe^{2+} couples, the galvanic exchange reaction is described via:

$$MnO_2 + 2Fe^{2+} + 4H^+ \rightarrow Mn^{2+} + 2Fe^{3+} + 2H_2O$$

Besides, our results show that the Fe galvanic exchange reaction also resulted in a morphology transformation of the initial HMO nanosheet assemblies to nanocones (Fig. 1c and d) in FMO1 and FMO2 as indicated with arrows in Fig. S3a–d.† Interestingly, this morphology was only observed in the materials with relatively lower amount of Fe^{2+} ions used, thus indicating that the transformation is sensitive to the ratio of Fe^{2+} ions used during galvanic exchange reaction.

The nanocones clearly show the characteristic hexagonal pyramid shape with faceted faces. The average nanocone lengths of FMO1 and FMO2 are 230 ± 89 nm and 279 ± 100 nm with corresponding basal widths of 87 ± 32 nm and 184 ± 73 nm, respectively (Fig. S4†). Furthermore, unlike these hollow shaped nanocones, nanocones with a closed tip could be distinguished as minority (Fig. S5†). This can be a result of the pyramidal growth of nanocones one inside the other and subsequent break of the structure into individual cones.[22]

Since the pH is known to affect the morphology/phase transformation of manganese oxides[17] the pH of the MnO_2 and Fe solutions was measured prior to galvanic exchange reaction. In all cases, the pH was close to neutral (pH $\approx$ 7) (Fig. S6a†). Strong changes in pH could force different morphology/phase transitions as a result from the galvanic exchange reaction, as seen in Fig. S6b† for the case of conducting FMO3 in basic pH (pH $\approx$ 10.5, adjusted with TMAOH). Fig. S6c† demonstrates that the presence of TMA cations is not responsible for the different transition, as FMO3 experiments with equivalent presence of TMA^+ in neutral pH do not modify the nanosheet morphology.

Evaluation of the capacitance properties of nanosheets and nanocones

CVs of 2D MnO_2 (HMO) and a $Fe_xMn_{1-x}O_2$ nanocone-rich material (1M-FMO2, see Section 5) were measured in the potential range of 0.21–1.01 V vs. the standard hydrogen electrode (SHE). SEM micrographs of the two electrodes can be found in Fig. S7.† To investigate the effect of the morphology transformation on the capacitive properties, the specific differential capacitance was calculated from the CV data obtained in three distinct measurements, averaged and plotted against the potential (Fig. 2). Despite the presence of ohmic-drop-related distortions of the CVs (particularly for 1M-FMO2) obstructing a quantitative comparison between both data sets, higher specific capacitance of HMO is observed in most part of the analyzed potential range.

24192 | J. Mater. Chem. A, 2022, 10, 24190–24198

This journal is © The Royal Society of Chemistry 2022

Paper

Fig. 2 Averaged specific differential capacitance of 2D MnO_x nanosheets (HMO) and nanocone-rich $Fe_xMn_{1-x}O_2$ (1M-FMO2) sample. The standard deviation was used to obtain the error bar reported in the plot.
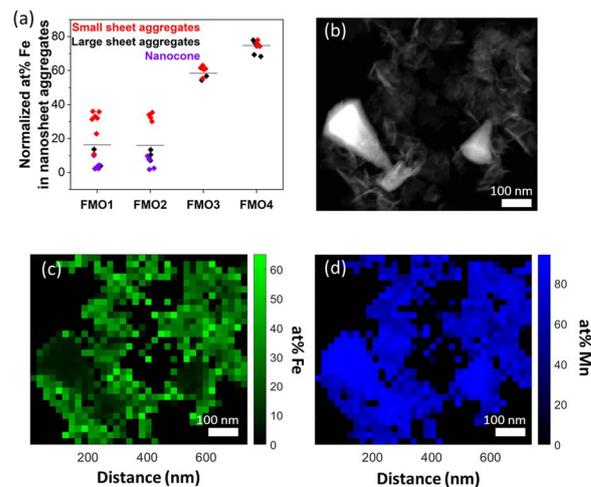

Fig. 3 (a) Normalized at% Fe with respect to at% Mn for each material. (b–d) HAADF micrograph and corresponding EDS mapping after PCA analysis showing the distribution of Fe and Mn on nanosheets and nanocones in FM02.

We hypothesize that this difference may arise from a different accessibility of the material for charge compensating ions. The hexagonal pyramid morphology of the nanocones present in 1M-FMO2 likely results in a decreased accessible surface area when compared to the 2D nanosheet morphology of HMO. The Fe content could also play a role in the differences and mechanism of the capacitive (dis-)charging (Fig. S8†). Furthermore, the lower capacitances could also indicate a transition to a different crystal structure with less favorable capacitance properties than δ-MnO_2.[27,28] The distinctive capacitance behavior of the nanocones compared to that of nanosheets highlights the importance of understanding the paths of morphology transitions for the rational design of functional materials. To gain mechanistic insights, the transformation was further studied by thorough characterization of the nanostructures.

Composition and oxidation state analyses

EDS was conducted in STEM mode on all the FMO materials to determine the Fe contents of the different nanostructures, i.e. assembled nanosheets or nanocones. The results are summarized on Fig. 3a. The average at% Fe of the assembled nanosheets were 20, 20, 56 and 75% for FMO1, FMO2, FMO3 and FMO4, respectively. Although the Fe content on FMO3 and FMO4 was relatively homogeneous, FMO1 and FMO2 showed higher scattering of Fe concentration from various regions of analysis. Smaller 3D nanosheet assemblies (<500 nm) tend to possess higher Fe content than larger assemblies. Additionally, in case of larger assemblies, nanosheets in outer area (or surface) showed higher Fe content than those in inner part (or core) (Fig. S9†). From this we believe that upon low amount of Fe^{2+}, these ions could not diffuse into the inner part of the thicker nanosheet assemblies.

Analyses of the nanocone structure in both FMO1 and FMO2 revealed that those barely contain an average of 5 at% Fe, a much lower value compared to the 20 at% Fe of the assembled nanosheets of the same samples. Local differences of up to

a ∼50 at% Fe between nanocones and nanosheets are shown quantitatively with a principle component analysis (PCA) of the EDS map data[29] on Fig. 3b–d. This suggests that nanocones may consist of a different crystal structure than the assembled nanosheets by terms of chemical component as well as morphology.

EELS measurements were conducted in STEM mode on all the $Fe_xMn_{1-x}O_2$ (FMO) materials to determine the oxidation state of the metal ions in the structure. The intensity ratios between L_2 and L_3 white lines ($I(L_3)/I(L_2)$) as well as the Fe $L_{2,3}$ and Mn $L_{2,3}$ peak positions are indicators of the average oxidation state of the element, with shifts towards larger energy losses indicating higher oxidation states.[30,31] However, the Fe L_3 peak position is maintained stable at ∼710.2 eV for all materials while the Fe $I(L_3)/I(L_2)$ ratio only suffers from a slight change (Fig. S10,† Table 1). All the intensity ratio values are close to the reported $I(L_3)/I(L_2) \approx 5.1$ for α-Fe_2O_3,[32] thus suggesting a dominance of Fe^{3+} oxidation state in all nanosheet specimens. This result is consistent with the galvanic exchange reaction transforming all Fe^{2+} precursor to Fe^{3+}.

Unlike Fe, the oxidation state of Mn varies. Fig. 4a contains the Mn L_3 EELS spectra for assembled nanosheets of HMO,

Table 1 EELS values for Fe and Mn L_3 white lines maxima and Fe and Mn $I(L_3)/I(L_2)$ intensity ratio for nanosheets and nanocones of HMO, FMO1, FMO2, FMO3 and FMO4

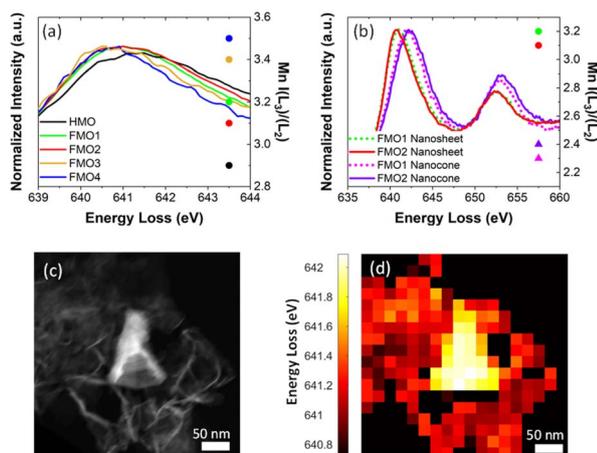| Material		Fe L_3 (eV)	Fe $I(L_3)/I(L_2)$	Mn L_3 (eV)	Mn $I(L_3)/I(L_2)$
HMO nanosheet		—	—	641.5	2.9
FMO1	Nanosheet	710.2	5.4	641.1	3.2
	Nanocone	—	—	642.2	2.3
FMO2	Nanosheet	710.2	5.4	641.1	3.1
	Nanocone	—	—	642.4	2.4
FMO3 nanosheet		710.2	5.2	640.8	3.4
FMO4 nanosheet		710.2	5.5	640.7	3.5

Fig. 4 (a) Left-Y axis: EELS Mn L_3 white line of the nanosheets of each material. Right-Y axis: intensity ratio of Mn L_3 and L_2 peaks (b) Left-Y axis: EELS Mn $L_{2,3}$ white lines of nanosheets and nanocones of FMO1 and FMO2. Right-Y axis: intensity ratio of Mn L_3 and L_2 peaks for FMO1 and FMO2 nanocones and nanosheets. (c and d) HAADF and corresponding EELS mapping after PCA analysis showing the local energy loss corresponding to Mn L_3 of the nanosheets and nanocones.

FMO1, FMO2, FMO3 and FMO4. The spectra show a shift of Mn L_3 between the materials with Fe (Table 1) and HMO, indicating that upon galvanic exchange there are enhanced contributions of lower Mn valences (Mn^{3+}/Mn^{2+}) due to the partial substitution of Mn^{4+} by Fe^{3+}. These qualitative results were also confirmed by $I(L_3)/I(L_2)$ ratios, the reference values of which decrease from $I(L_3)/I(L_2)_{MnO} \approx 4.0$, $I(L_3)/I(L_2)_{Mn_2O_3} \approx 2.5$ to $I(L_3)/I(L_2)_{MnO_2} \approx 1.9$.[30] The calculated ratios shown in Fig. 4a and Table 1 increase from 2.9 to 3.5 with Fe, thus showing more reduction following the higher Fe content.

The value of $I(L_3)/I(L_2)_{HMO} \approx 2.9$ indicates that the Mn ions in HMO before addition of Fe are already in a very low valence, with significant Mn^{2+}/Mn^{3+} contributions. This is compatible with a birnessite structure containing hydrated cations in the interlayer to compensate Mn^{3+}/Mn^{4+} or Mn^{2+}/Mn^{4+} of the structure, characteristic of the synthesis methodology.[33,34]

EELS spectra show a Mn L_3 peak shift as high as ~1.1 eV for FMO1 and ~1.3 eV for FMO2 between nanocones and nanosheets (Fig. 4b, Table 1). This difference is also seen by local PCA of an EELS mapping of a nanocone and nanosheets[29] (Fig. 4c and d) with data displaying the energy loss of the Mn L_3 peak maximum as indicator of oxidation state. Such results clearly reveal that Mn ions in the nanocones are more oxidized than those in assembled nanosheets. This is confirmed by the distinct changes of intensity ratios from $I(L_3)/I(L_2)_{FMO1} \approx 3.2$ and $I(L_3)/I(L_2)_{FMO2} \approx 3.1$ for nanosheets to $I(L_3)/I(L_2)_{FMO1} \approx 2.3$ and $I(L_3)/I(L_2)_{FMO2} \approx 2.4$ for nanocones. The magnitude of the difference between Mn oxidation state in assembled nanosheets and nanocones can neither be explained solely by the different Fe content nor by a difference in their thicknesses (Fig. S2†). Therefore, these results strongly indicate the oxidation of the Mn ions during morphology transformation from 2D MnO_2 nanosheet to nanocones.

Crystal structure

To elucidate the crystal structure of the materials, confocal Raman spectroscopy measurements were conducted (Fig. 5). All the spectra show four active modes: $\nu 1$ (721.6–744.9 cm^{-1}), $\nu 2$ (636.2–643.0 cm^{-1}), $\nu 3$ (566.9–573.0 cm^{-1}), and $\nu 4$ (487.1–500.8 cm^{-1}) (Table S1†). These modes can be assigned to the layered birnessite δ-MnO_2 structure for all FMO1, FMO2, FMO3 and FMO4 despite the different Fe contents.[8,34,35] X-ray diffraction (XRD) also confirmed such phase in HMO (Fig. S11†).

Moreover, Raman $\nu 1$ and $\nu 2$ modes appear broader in the materials with higher Fe contents (FMO3 and FMO4). This result is compatible with a higher extend of galvanic exchange reaction with higher Fe ratios, which induces the formation of more Mn defects and Mn^{2+} cations. Such defects reduce the order of the lattice, resulting in a polycrystalline structure with smaller grain sizes which broaden the Raman peaks.[34] The smaller grain size of the materials with higher Fe content was also confirmed by TEM imaging the materials (Fig. S12†).

Local crystal structure investigations of the nanocones and the nanosheets were conducted by HRTEM, Fast Fourier Transform (FFT) (Fig. 6a–f and S13†) and selected area aperture electron diffraction (SAED) (Fig. 6g and h). The data indicates that the assembled nanosheets of HMO as well as nanosheets containing Fe (FMO1, FMO2, FMO3 and FMO4) show a polycrystalline birnessite structure (Fig. S14†) while nanocones are highly crystalline e.g. much larger crystal size. The nanocone
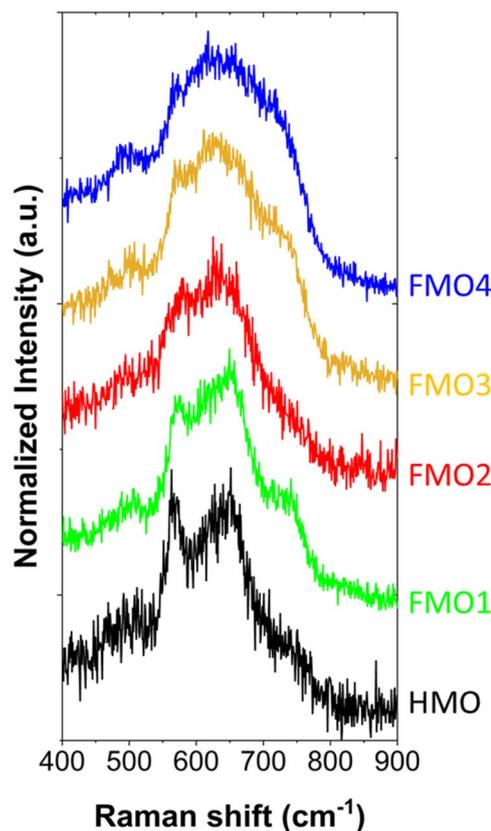

Fig. 5 Raman spectra of HMO, FMO1, FMO2, FMO3 and FMO4.

24194 | J. Mater. Chem. A, 2022, **10**, 24190–24198

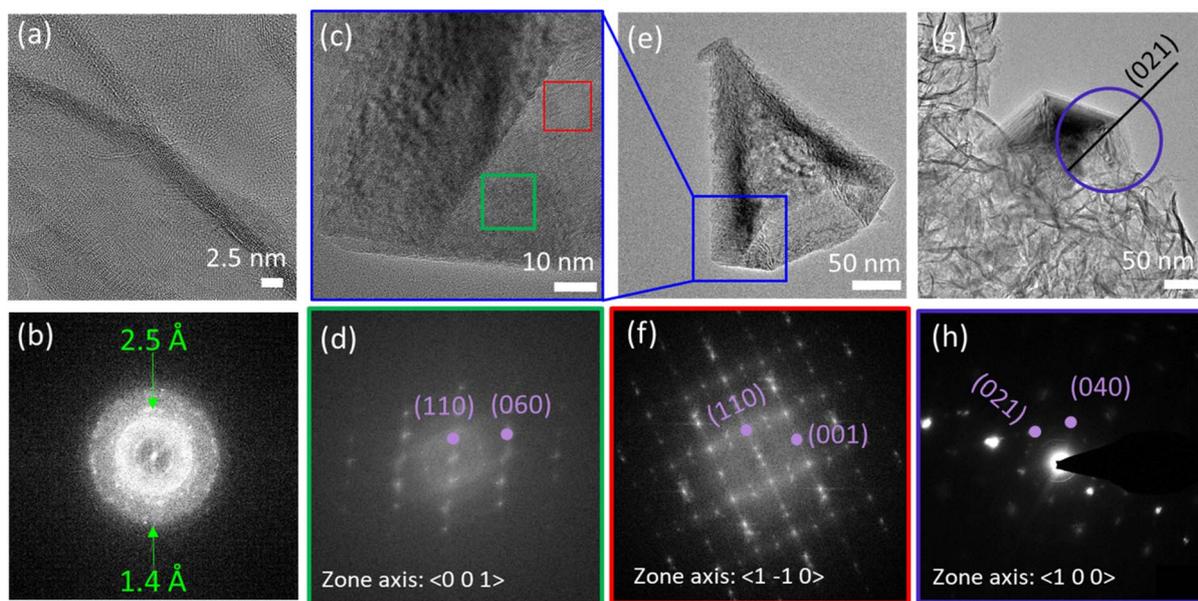This journal is © The Royal Society of Chemistry 2022

Fig. 6 (a and b) HRTEM micrograph and corresponding FFT pattern of a HMO nanosheet. (c–f) HRTEM micrographs and FFT patterns corresponding to two facets of a FMO2 nanocone. (g and h) TEM micrograph and corresponding SAED pattern of a FMO2 nanocone.

patterns could be assigned to the γ-MnO$_2$ ramsdellite crystal structure (orthogonal phase with $a = 4.51$, $b = 9.26$, $c = 2.86$, space group Pbnm (62)), in agreement with previous reports.[21] The nanocone planes were determined to be the (1–10) for the facets of the nanocone with a twinning along the $\langle 021 \rangle$ direction and the (100) facet on the base. This confirms that a coupled morphology and phase transition occurs upon Fe galvanic exchange reaction.

Nanocone growth mechanism from galvanic exchange reaction

With the results of the morphological and chemical analyses of Fe$_x$Mn$_{1-x}$O$_2$ nanosheets and nanocones, we hypothesize the following mechanism for the coupled morphology/phase transformation (Fig. 7). During the galvanic exchange reaction, Fe^{2+} reduces Mn^{4+}, yielding Fe^{3+} and Mn^{2+}. The fate and equilibrium of these cations is key for obtaining one morphology or the other. As demonstrated by the EDS analyses, when the initial Fe^{2+} to MnO$_2$ nanosheets ratio is high, the only outcome are nanosheets with large Fe contents (FMO3 and FMO4). This means the Fe^{3+} occupies most of the available positions in the lattice, interlayer, and adsorption sites on the surface of MnO$_2$ nanosheets while Mn^{2+} is dissolved in aqueous solution, yielding Fe$_x$Mn$_{1-x}$O$_2$ nanosheets as the only product. The partial dissolution of Mn^{4+} to Mn^{2+} as a consequence of Fe galvanic exchange reaction was demonstrated by performing ICP-MS on the solutions after reaction of MnO$_2$ with Fe. The results showed larger amounts of Mn ions in the materials with larger amounts of Fe precursor (Table S2†).

The morphological and EDS analyses revealed the phase transformation at lower Fe^{2+} to MnO$_2$ nanosheets ratio. At such conditions, a competition between Fe^{3+} and Mn^{2+} for the lattice and interlayer sites can occur and Mn^{2+} will also partially

occupy those sites instead of completely dissolving in solution. Upon aging for 24 h of the materials, these Mn^{2+} cations will be re-oxidized by atmospheric and water-dissolved oxygen, yielding γ-MnO$_2$ nanocones with low Fe contents and higher Mn oxidation states, as demonstrated by EDS and EELS analyses. Since the oxidation state of the starting layered MnO$_2$ nanosheet is lower than that of the nanocone product, a comproportionation mechanism for this transformation can be discarded.

To confirm the key role of the *in situ* Mn^{2+} formation we tried to reproduce the results of FMO2 by substituting Fe^{2+} for an equivalent molar percentage of Mn^{2+} (MMO2, Fig. S15†). A morphology transformation was successfully produced by Mn^{2+}, confirming it is triggered by such cation. Although the EELS and Raman analysis showed similar results in MMO2 as compared to FMO2 (Fig. S16†), instead of obtaining a defined nanocone shape the MMO2 nanostructures showed a small faceted cone-like nanoparticle morphology. This contrast with the previous results reported by Tu *et al.*,[17] who could obtain nanosheet to nanocone transformation through Mn^{2+} adsorption, can be explained by their much longer aging times. Such finding highlights the role of Fe^{2+} in speeding up the transformation by generating *in situ* the Mn^{2+} species with crystal defects, thus reducing the time of synthesis of well-defined nanocones.

Finally, since the nanocone transformation occurs through an oxidative step, the original oxidation state of the 2D MnO$_2$ (HMO) can be of upmost importance. To assess its effect, three 2D MnO$_2$ materials named 1M-HMO, 2M-HMO and 3M-HMO were synthesized by modifying the synthesis and aging time (see Experimental section) in order to change their Mn oxidation state. This was monitored by EELS (Fig. 8a), demonstrating
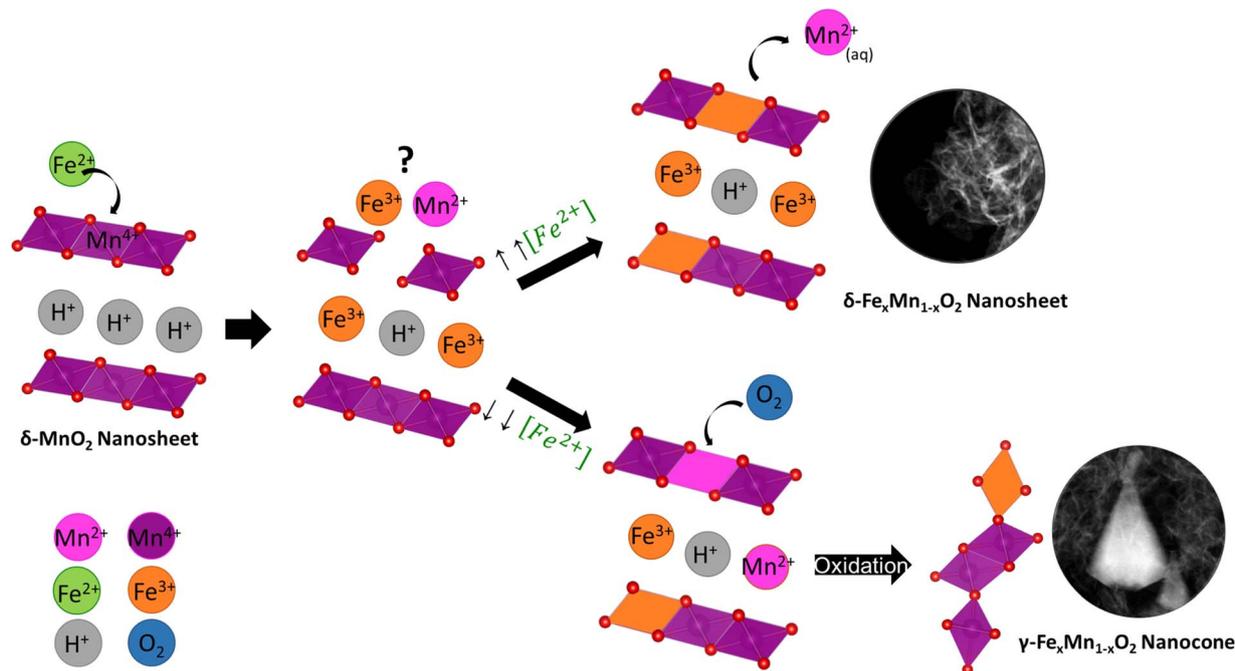
This journal is © The Royal Society of Chemistry 2022

J. Mater. Chem. A, 2022, **10**, 24190–24198 | **24195**

Fig. 7 Schematic mechanism governing the synthesis of $Fe_xMn_{1-x}O_2$ nanosheets and nanocones through galvanic exchange reaction.
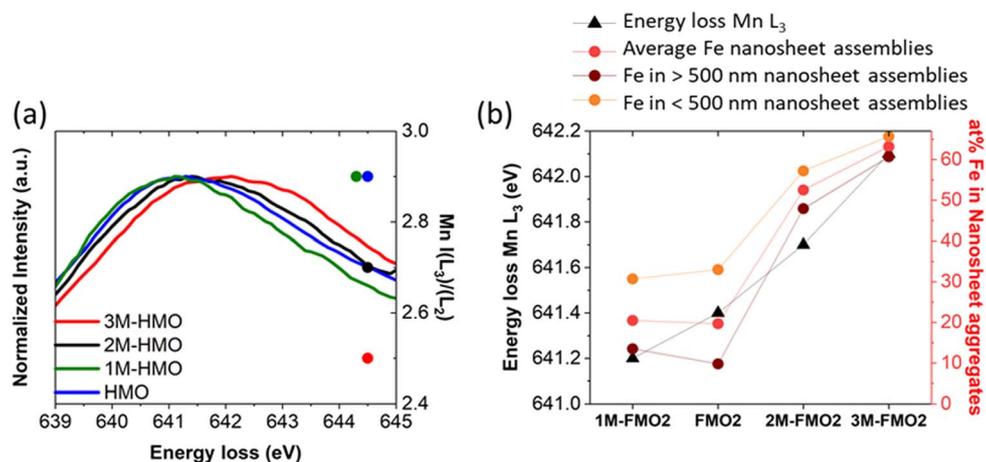

Fig. 8 (a) Left-Y Axis: EELS Mn L_3 peaks of HMO, 1M-HMO, 2M-HMO and 3M-HMO. Right-Y axis: corresponding Mn $I(L_3)/(L_2)$ values. (b) Trends of oxidation state of xM-HMO (Left-Y axis) and Fe introduced by galvanic exchange reaction (right-Y axis) for xM-FMO2.

that the longer the synthesis and aging times, the more oxidized the Mn species of the 2D MnO_2 nanosheets.

Galvanic exchange reaction was subsequently conducted with these xM-HMO materials emulating FMO2 conditions (xM-FMO2). The results showed that the materials produced with more oxidized MnO_2 nanosheets (2M-FMO2 and 3M-FMO2) contained $Fe_xMn_{1-x}O_2$ nanosheets with larger contents of Fe than FMO2 but containing similar ratio of nanocones (Fig. 8b and S17†). On the contrary, reducing the oxidation state of Mn species (1M-HMO) by shorter synthesis and aging time resulted on materials with the same 20 at% Fe than HMO after galvanic exchange reaction. However, the difference in oxidation state of 1M-HMO contributed to the major enhancement of the

nanocone morphology with respect to nanosheet after reaction (Fig. S17†). These results can be related to the galvanic exchange reaction potentials with different Mn^{n+} species. The reaction between Fe^{3+}/Fe^{2+} and Mn_2O_3/Mn^{2+} couples is thermodynamically more favourable than that of Fe^{3+}/Fe^{2+} and MnO_2/Mn^{2+} ($\Delta E^0_{cell} = 0.714$ V $vs. \Delta E^0_{cell} = 0.459$ V, respectively). This difference potentially indicates larger local concentration of produced Mn^{2+} during galvanic exchange reaction with the more reduced 1M-HMO due to the higher thermodynamic driving force, explaining the larger nanocone to nanosheet ratio. Moreover, the nanocone size is also larger, showing an average length 391 ± 197 nm and average width 228 ± 91 nm distributed in two different family sizes. (Fig. S4†).

24196 | J. Mater. Chem. A, 2022, **10**, 24190–24198

This journal is © The Royal Society of Chemistry 2022

Conclusions

A rapid layer-to-tunnel transformation from δ-MnO_2 nanosheets to γ-MnO_2 nanocones was achieved via Fe galvanic exchange reaction. Such transformation leads to a change of the electrochemical capacitive properties of the $Fe_xMn_{1-x}O_2$ nanomaterials. Mechanistic insights were gained by a combination of electron microscopy and spectroscopy techniques. According to local EELS analyses, the coupled morphology and phase transition followed an in situ Mn^{2+} generation and reoxidation mechanism. Investigations on the oxidation state of the MnO_2 nanosheets and the ratio between Fe^{2+} and MnO_2 for galvanic exchange reaction revealed the major role of the equilibrium between the generated Mn^{2+} and Fe^{3+} cations for the layer-to-tunnel transition, allowing to tune the nanostructures obtained. This work highlights the importance of mechanistic understanding for the rational design, synthesis, and structure–property relationships of functional nanomaterials.

Author contributions

R. A. A. conducted the synthesis, electron microscopy experiments and data analysis and was assisted by J. L. (J. Lim) and C. S. for the results interpretation. P. C. and R. A. A. performed the electrochemical measurements. K. T. and J. L. (J. Linnenmann) assisted in the interpretation of the electrochemistry data. P. E. conducted the Raman spectroscopy experiments which were analyzed and interpreted by R. A. A. and M. R. R. A. A. wrote the manuscript with contributions of all authors. All authors have given approval to the final version of the manuscript.

Conflicts of interest

There are no conflicts to declare.

Acknowledgements

References

1 C. M. Julien and A. Mauger, Nanomaterials, 2017, 7, 396.

2 R. Yang, Y. Fan, R. Ye, Y. Tang, X. Cao, Z. Yin and Z. Zeng, Adv. Mater., 2021, 339, 2004862.

3 Y. Meng, W. Song, H. Huang, Z. Ren, S.-Y. Chen and S. L. Suib, J. Am. Chem. Soc., 2014, 136, 11452–11464.

4 P. K. Gupta, A. Bhandari, S. Saha, J. Bhattacharya and R. G. S. Pala, J. Phys. Chem. C, 2019, 123, 22345–22357.

5 Z. Ye, T. Li, G. Ma, Y. Dong and X. Zhou, Adv. Funct. Mater., 2017, 27, 1704083.

6 L. Tian, X. Zhai, X. Wang, J. Li and Z. Li, J. Mater. Chem. A, 2020, 8, 14400–14414.

7 M. H. Oh, T. Yu, S.-H. Yu, B. Lim, K.-T. Ko, M.-G. Willinger, D.-H. Seo, B. H. Kim, M. G. Cho, J.-H. Park, K. Kang, Y.-E. Sung, N. Pinna and T. Hyeon, Science, 2013, 340, 964–968.

8 J. Lim, J. M. Lee, B. Park, X. Jin and S.-J. Hwang, Nanoscale, 2017, 9, 792–801.

9 H. Liu, W. Gu, B. Luo, P. Fan, L. Liao, E. Tian, Y. Niu, J. Fu, Z. Wang, Y. Wu, G. Lv and L. Mei, Electrochim. Acta, 2018, 291, 31–40.

10 D. P. Dubal, W. B. Kim and C. D. Lokhande, J. Phys. Chem. Solids, 2012, 73, 18–24.

11 Y. Wang, Y.-Z. Zhang, Y.-Q. Gao, G. Sheng and J. E. ten Elshof, Nano Energy, 2020, 68, 104306.

12 S. Birgisson, D. Saha and B. B. Iversen, Cryst. Growth Des., 2018, 18, 827–838.

13 T. Hatakeyama, H. Li, N. L. Okamoto, K. Shimokawa, T. Kawaguchi, H. Tanimura, S. Imashuku, M. Fichtner and T. Ichitsubo, Chem. Mater., 2021, 33, 6983–6996.

14 D. A. Kitchaev, S. T. Dacek, W. Sun and G. Ceder, J. Am. Chem. Soc., 2017, 139, 2672–2681.

15 Y.-F. Li, S.-C. Zhu and Z.-P. Liu, J. Am. Chem. Soc., 2016, 138, 5371–5379.

16 B. He, G. Cheng, S. Zhao, X. Zeng, Y. Li, R. Yang, M. Sun and L. Yu, J. Solid State Chem., 2019, 269, 305–311.

17 S. Tu, G. J. Racz and T. B. Goh, Clays Clay Miner., 1994, 42, 321–330.

18 P. Yang, S. Lee, J. E. Post, H. Xu, Q. Wang, W. Xu and M. Zhu, Geochim. Cosmochim. Acta, 2018, 240, 173–190.

19 E. J. Elzinga, Environ. Sci. Technol., 2011, 45, 6366–6372.

20 Y. Yuan, K. He, B. W. Byles, C. Liu, K. Amine, J. Lu, E. Pomerantseva and R. Shahbazian-Yassar, Chem, 2019, 5, 1793–1805.

21 D. Portehault, S. Cassaignon, E. Baudrin and J.-P. Jolivet, Cryst. Growth Des., 2009, 9, 2562–2565.

22 Y.-S. Ding, X.-F. Shen, S. Gomez, H. Luo, M. Aindow and S. L. Suib, Adv. Funct. Mater., 2006, 16, 549–555.

23 D. Portehault, S. Cassaignon, E. Baudrin and J.-P. Jolivet, J. Mater. Chem., 2009, 19, 7947–7954.

24 K. Kai, Y. Yoshida, H. Kageyama, G. Saito, T. Ishigaki, Y. Furukawa and J. Kawamata, J. Am. Chem. Soc., 2008, 130, 15938–15943.

25 F. Karnbach, M. Uhlemann, A. Gebert, J. Eckert and K. Tschulik, Electrochim. Acta, 2014, 123, 477–484.

26 P. A. van Aken and B. Liebscher, Phys. Chem. Miner., 2002, 29, 188–200.

27 S. Devaraj and N. Munichandraiah, J. Phys. Chem. C, 2008, 112, 4406–4417.

28 T. Brousse, M. Toupin, R. Dugas, L. Athouël, O. Crosnier and D. Bélanger, J. Electrochem. Soc., 2006, 153, A2171.

This journal is © The Royal Society of Chemistry 2022

J. Mater. Chem. A, 2022, 10, 24190–24198 | 24197

29 S. Zhang and C. Scheu, *Microsc*, 2017, **67**, i133–i141.

30 H. Tan, J. Verbeeck, A. Abakumov and G. Van Tendeloo, *Ultramicroscopy*, 2012, **116**, 24–33.

31 J. Lim, X. Jin, S.-J. Hwang and C. Scheu, *Adv. Funct. Mater.*, 2020, **30**, 2003849.

32 C. Wang, Y. Wang, X. Liu, H. Yang, J. Sun, L. Yuan, G. Zhou and F. Rosei, *Nanotechnology*, 2015, **27**, 035702.

33 S. Min and Y. Kim, *Minerals*, 2020, **10**, 884.

34 C. Julien, M. Massot, R. Baddour-Hadjean, S. Franger, S. Bach and J. P. Pereira-Ramos, *Solid State Ionics*, 2003, **159**, 345–356.

35 C. M. Julien, M. Massot and C. Poinsignon, *Spectrochim. Acta, Part A*, 2004, **60**, 689–700.

24198 | *J. Mater. Chem. A*, 2022, **10**, 24190–24198

This journal is © The Royal Society of Chemistry 2022